

Differential cross sections of the charge-exchange reaction $\pi^-p \rightarrow \pi^0n$ in the momentum range from 103 to 178 MeV/c

D. Mekterović,^{1,*} I. Supek,¹ V. Abaev,² V. Bekrenev,² C. Bircher,³ W. J. Briscoe,⁴ R. V. Cadman,^{5,†} M. Clajus,⁶ J. R. Comfort,⁷ K. Craig,⁷ D. Grosnick,⁸ D. Isenhover,³ M. Jerkins,³ M. Joy,³ N. Knecht,⁹ D. D. Koetke,⁸ N. Kozlenko,² A. Kulbardis,² S. Kruglov,² G. Lolos,⁹ I. Lopatin,² D. M. Manley,¹⁰ R. Manweiler,⁸ A. Marušić,⁶ S. McDonald,⁶ B. M. K. Nefkens,⁶ J. Olmsted,^{10,‡} Z. Papandreou,⁹ D. Peaslee,^{11,§} J. Peterson,¹² N. Phaisangittisakul,⁶ S. N. Prakhov,⁶ J. W. Price,⁶ A. Ramirez,⁷ M. E. Sadler,³ A. Shafi,⁴ H. Spinka,⁵ S. Stanislaus,⁸ A. Starostin,⁶ H. M. Staudenmaier,¹³ I. Strakovsky,⁴ W. B. Tippens,⁶ and S. Watson³

(Crystal Ball Collaboration)

¹Ruder Bošković Institute, Zagreb 10000, Croatia

²Petersburg Nuclear Physics Institute, Gatchina 188350, Russia

³Abilene Christian University, Abilene, Texas 79699-7963, USA

⁴The George Washington University, Washington, DC 20052-0001, USA

⁵Argonne National Laboratory, Argonne, Illinois 60439-4815, USA

⁶University of California, Los Angeles, California 90095-1547, USA

⁷Arizona State University, Tempe, Arizona 85287-1504, USA

⁸Valparaiso University, Valparaiso, Indiana 46383-6493, USA

⁹University of Regina, Saskatchewan, Canada S4S 0A2

¹⁰Kent State University, Kent, Ohio 44242-0001, USA

¹¹University of Maryland, College Park, Maryland 20742-4111, USA

¹²University of Colorado, Boulder, Colorado 80309-0390, USA

¹³Universität Karlsruhe, Karlsruhe 76128, Germany

(Dated: December 13, 2018)

Measured values of the differential cross sections for pion-nucleon charge exchange, $\pi^-p \rightarrow \pi^0n$, are presented for π^- momenta of 103, 112, 120, 130, 139, 152, and 178 MeV/c. Complete angular distributions were obtained by using the Crystal Ball detector at the Alternating Gradient Synchrotron at Brookhaven National Laboratory. Statistical uncertainties of the differential cross sections vary from 3% to 6% in the backward angle region, and from 6% to about 20% in the forward region with the exception of the two most forward angles. The systematic uncertainties are estimated to be about 3% for all momenta.

I. INTRODUCTION

There are three experimentally accessible scattering channels in the πN system: $\pi^+p \rightarrow \pi^+p$ and $\pi^-p \rightarrow \pi^-p$ elastic scattering, and the $\pi^-p \rightarrow \pi^0n$ charge-exchange reaction (CEX). Precise data for all three channels are needed to obtain an accurate description of the πN system via a consistent and complete set of scattering amplitudes. In that regard, the least satisfying situation is in the region below 100 MeV π^- kinetic energy where the experimental database for CEX is quite limited. On the other hand, the low-energy region is very interesting because isospin symmetry-breaking effects may be visible there. Furthermore, low-energy data have a strong impact on extrapolations of scattering amplitudes to the nonphysical region, and this extrapolation is needed to obtain important physical quantities such as the πN σ term.

Isospin symmetry is one of the key concepts in hadronic physics. Thus, it is very important to measure precisely small symmetry-breaking effects coming from both the up-down quark mass difference and the electromagnetic interaction. In the πN system, one such isospin-breaking effect is a departure from the so-called triangle relation

$$F_{CEX} = \frac{1}{\sqrt{2}}(F_+ - F_-), \quad (1)$$

*dmekter@irb.hr

†Present address: Wisconsin Institutes for Medical Research, Madison, Wisconsin 53705, USA

‡Present address: Lancaster General Hospital, Radiation Oncology, Lancaster, PA 17604 USA

§deceased

a relation between the scattering amplitudes for the CEX reaction and the two elastic channels. A surprisingly large 7% violation of the triangle relation was obtained at 40 MeV in an analysis by Gibbs, Ai, and Kaufmann [1]. As input, they used experimental data up to $T_\pi = 50$ MeV pion kinetic energy. A similar result was reported in independent work by Matsinos [2, 3] based on data up to $T_\pi = 100$ MeV. Fettes and Meissner [4] investigated isospin breaking in the framework of chiral perturbation theory up to 100 MeV/ c pion momentum and obtained only a 0.7% effect. A similarly small effect was also found by the George Washington University (GWU) group, Gridnev *et al.* [5]. Such a large discrepancy on this important question demands further investigation. From an experimental point of view, the weakest point is the lack of a sizeable set of data for low-energy CEX.

Among the quantities extracted from low-energy πN data, the πN σ term is distinguished both by its importance and by the lack of consensus on its precise value. For details, see [6] and references therein. The πN σ term is a measure of chiral symmetry breaking in the strong interaction. It is directly related to the strangeness content of the proton, and is also used in calculations of the mass spectra of hadrons and in searches for Higgs particles and dark matter. It is obtained by the extrapolation of the pion-nucleon scattering amplitudes to a negative energy point by taking advantage of their analytic properties. Charge-exchange data affect the determination of the σ term indirectly, but are important to provide a stable database to determine the amplitudes as close to threshold as possible before extrapolating to the non-physical region.

The first CEX data below 100 MeV come from an experiment that used a single large NaI detector [7], [8]. The detector was placed at seven angles and collected continuous γ energy spectra that were unfolded into CEX angular distributions, for six energies between 27.4 and 91.7 MeV. Fitzgerald *et al.* [9] used the Clinton P. Anderson Meson Physics Facility (LAMPF) π^0 spectrometer for coincident detection of the two π^0 decay photons. The experiment was performed at seven beam energies between 32.5 and 63.5 MeV and was restricted to laboratory polar angles smaller than 30° . Later measurements were made with the same detector at 10, 20, and 40 MeV that covered a larger selection of forward and backward angles, but these results were reported only as incomplete and preliminary [10]. Frlež *et al.* obtained differential cross sections at 27.5 MeV in an angular range between 0° and 55° [11]. A previous experiment by the Crystal Ball Collaboration [12] measured differential cross sections in the region dominated by Δ resonance. The two lowest energies in that experiment overlap with the two highest energies reported in this work.

The most recent published results are from Jia *et al.* [13]. They used the TRIUMF RMC spectrometer to obtain differential cross sections at six energies between 34.4 and 59.7 MeV in an angular range from 0° to 40° . Their motivation was to check the results of Fitzgerald *et al.*, especially in the context of isospin violation. Serious disagreement between the two experiments was found. Finally, an experiment by Breitschopf *et al.* [14] should also be mentioned. They did not measure differential cross sections but did provide total CEX cross sections at many energies in the Δ region, nine of which are below 100 MeV.

The results from the new experiment described in this paper add differential cross sections with full angular coverage (20 different angles) for seven energies from 34 to 87 MeV. Even if questions on the reliability of some of the previous experiments are ignored, these new data almost double the existing CEX data base below 100 MeV. Especially important is our contribution in the backward-angle region where we have small uncertainties and previous measurements are very scarce.

II. EXPERIMENTAL SETUP

The data presented in this work were measured in 2002 on the C6 beam line of the Alternating Gradient Synchrotron (AGS) at Brookhaven National Laboratory (BNL). The experiment (BNL experiment E958) was part of a program of baryon spectroscopy by the Crystal Ball Collaboration that included a long CEX run at higher energies in 1998. The experimental setups of 1998 and 2002 were very similar (with the most important parts such as the Crystal Ball detector, the veto barrel, data acquisition, *etc.* being identical). The experimental setup of the 1998 experiment is described in more detail in Ref. [15].

The main part of the experimental setup is the Crystal Ball (CB) detector, illustrated in Fig. 1. It is an electromagnetic calorimeter and spectrometer in the shape of a ball with a cavity in the center (which housed a target), and openings for beam entrance and exit. The openings reduce the geometric acceptance to 93% of 4π sr. The CB consists of 672 optically isolated NaI(Tl) crystals, each of them viewed by a single photomultiplier tube (PMT). The crystals are truncated triangular pyramids 5 cm on an edge at the inner radius, 13 cm at the outer radius, and 41 cm long.

The target used in the experiment was a cylinder 10 cm in diameter and 1 cm thick, composed of polyethylene (CH₂). Its downstream face was positioned in the center of the CB cavity. Data were also taken with a carbon target of the same shape, size, and position in order to subtract the background produced by scattering and interaction of pions on carbon nuclei. Remaining beam related backgrounds were subtracted by using data taken without a target.

A veto barrel (VB) was installed to reject events that had charged particles in the final state. It was constructed of

four curved plastic scintillators that formed a cylindrical shell around the beam pipe. The beam pipe was a cylindrical aluminum support element placed through the beam opening of the CB. Each segment of the VB was 5 mm thick and 120 cm long. Each end of the four segments was viewed by a photomultiplier tube.

There were five plastic scintillators, a set of drift chambers, and a gas Čerenkov counter along the beam line. The first scintillator S1 on the beam line was positioned before the last bending magnet D2. All signals were timed with respect to an ST scintillator that was placed 160 cm upstream from the target. Beam normalization was achieved with a small 5-cm-by-5-cm scintillator, called SB, inserted 30 cm upstream from the target. All three scintillators were viewed by two PMTs (left and right). A coincidence between S1, ST, and SB defined the beam. For time-of-flight (TOF) analysis, another scintillator, designated BVS, was also used. It was positioned 210 cm downstream of the target. The Čerenkov counter was moved upstream from its position in the 1998 experiment and positioned just after the BVS. It was used to measure the electron contamination of the beam. Beam trajectories were measured by the six drift chambers (three for the horizontal coordinate and three for the vertical coordinate). A drift chamber before D2 was used to determine the difference in momentum of the beam particle from the central value set by the beam tune.

Data collected with a pulser trigger (random trigger), a beam trigger, a charged trigger, and a neutral trigger were used in the analysis. The beam trigger was defined as a coincidence between signals from S1, ST, and SB:

$$Beam = S1 \cdot ST \cdot SB. \quad (2)$$

Data collected with this trigger were used in beam normalization studies. Both the charged and the neutral trigger included the beam requirement mentioned above. In addition, they required that the total energy in the CB should be above 75 MeV. These triggers differed as to whether they included the existence of a signal from the veto barrel. Thus, the charged trigger was defined as

$$Ch. = Beam \cdot (E_{CB} > 75 \text{ MeV}) \cdot VB, \quad (3)$$

and the neutral trigger

$$Neut. = Beam \cdot (E_{CB} > 75 \text{ MeV}) \cdot \overline{VB}. \quad (4)$$

The charged trigger was needed for calibration of the VB, and the neutral trigger was our primary trigger from which cross sections were calculated. All triggers except the neutral trigger were prescaled.

III. DATA ANALYSIS

The differential cross sections were calculated by using the expression

$$\frac{d\sigma}{d\Omega} = \frac{1}{\Delta\Omega t \epsilon} \left[\frac{Y_{CH2}}{N_{CH2}^{\pi^-}} - r_c r_\epsilon F \frac{Y_C}{N_C^{\pi^-}} - (1 - r_c r_\epsilon F) \frac{Y_E}{N_E^{\pi^-}} \right], \quad (5)$$

where the indices CH2, C, and E refer to data taken with the polyethylene target, carbon target, or no target, respectively; Y is the number of detected π^0 s; N_{π^-} is the number of beam π^- s incident on a target and corrected for live time; r_c is the ratio of the numbers of carbon nuclei in the CH2 and C targets; r_ϵ is the ratio of acceptances for scattering on carbon nuclei for the CH2 and C targets; F is a small correction factor to compensate for differences between the average π^- momenta in the CH2 and carbon targets; ϵ is the acceptance for the CH2 target; t is proton areal density in the CH2 target; and $\Delta\Omega$ is the size of the solid angle bin.

The proton area density, t , and ratio r_c were determined from the target specifications, and the size of the solid angle bin is given by the number of bins.

The CH2 and carbon targets had the same length, but the carbon target was more dense so the average π^- momentum in it was lower than the average momentum for the CH2 target by 0.6 MeV/c to 1.3 MeV/c, going from the highest to the lowest momentum. This shift led to a correction factor F :

$$\frac{d\sigma_C}{d\Omega}(p_{CH2}) = F \frac{d\sigma_C}{d\Omega}(p_C), \quad (6)$$

which is a ratio of differential cross sections for CEX on carbon nuclei at the momenta in the CH2 and carbon targets. The values for F were estimated from the data for the carbon target. They were found to vary from about 1.005 to about 1.05, going from the highest to the lowest momentum. The uncertainty of this estimate was taken to be $(F - 1)/2$ and was included in the estimate of the systematic uncertainty.

Calculation of the remaining quantities in Eq. 5, together with the precise determination of beam momenta, is described in the following sections. As mentioned in the Introduction, our collaboration has already published CEX data, Sadler *et al.* [12], in the Δ region, partially overlapping in energy with the experiment reported here. The analysis here is very similar to that of Sadler *et al.*, and we will refer to it for some aspects of the analysis.

TABLE I: Definitions of tests used in reconstruction of π^0 s. Opening angle and TOF cuts are momentum dependent.

Test	Definition
Neutral trigger	$S1 \cdot ST \cdot SB \cdot (E_{CB} > 75 \text{ MeV}) \cdot \overline{VB}$
Invariant mass	Only one cluster pair with: $105 \text{ MeV}/c^2 < M_I < 155 \text{ MeV}/c^2$
Missing mass	For π^0 cluster pair: $917 \text{ MeV}/c^2 < M_M < 955 \text{ MeV}/c^2$
Opening angle	For π^0 cluster pair: $\theta > \theta_{\min}$
Number of clusters	$N_c \leq 3$
Geometry cut	Beam-in tunnel region excluded for π^0 clusters
CB energy without tunnel region	$E_{CB}^{in} > 80 \text{ MeV}$
TOF	$TDC_{SB} - TDC_{S1} > TDC_{\min}$

A. Detection of π^0 s

Data taken with the carbon target and no target were analyzed in the same way as data with the CH2 target and were subtracted from the CH2 data as given by Eq. 5. In this way, the carbon background and accidental backgrounds were removed. The only other possible source of background would be pion radiative capture, $\pi^- p \rightarrow \gamma n$, but Monte Carlo analysis showed that it contributed less than 0.2% and it was thus ignored.

The $\pi^- p \rightarrow \pi^0 n$ reaction was identified in the subset of data collected with a neutral trigger by measuring the energy and direction of the two photons from $\pi^0 \rightarrow \gamma\gamma$ decay. Each photon produced an electromagnetic shower in the CB that spread over several neighboring crystals. The first step in the analysis was to find such sets of crystals, called clusters. In a cluster-finding algorithm, a set of crystals with a deposited energy greater than 7 MeV was found. Such crystals, if not neighboring each other, were declared as a central crystal. A cluster was then defined to be the central crystal and its 21 neighbors with the condition that the total energy of the four highest-energy crystals in the cluster should be at least 17.5 MeV. The position of the cluster was the weighted average of positions of the crystals in the cluster, where the weighting factor was the square root of the deposited energy.

Once the energies and positions of all clusters were found, a number of cuts were applied to select the CEX events. Because detection of π^0 s required detection of both photons from the decay, at least two clusters were needed. A third cluster could come from the neutron, so events with three clusters were included but events with more than three clusters were rejected. This cut suppressed accidental backgrounds. The most important cut, the signature of the CEX reaction, is that the invariant mass of only one pair of clusters (for 3-cluster events there are 3 pairs of clusters) be equal, within experimental resolution, to the π^0 mass.

A very important cut is one on the missing mass because it strongly suppresses the carbon background. For CEX reactions on a proton target, the missing mass is equal to the neutron mass, while for the background reaction on carbon nuclei it is somewhat higher. Requiring that the missing mass be less than $955 \text{ MeV}/c^2$ reduces the carbon background by about half and thus further reduces statistical and systematic uncertainties. This very strong cut changed the total cross section (due to a small difference between real and Monte Carlo data) by 1% - 2%. This change was included in the estimate of systematic uncertainties. Accidental backgrounds, because they were beam related, had the strongest impact on crystals in the region surrounding the beam entrance or exit. In the final analysis, the beam entrance was excluded for clusters reconstructed to come from π^0 .

Other cuts designed to suppress backgrounds include one cut on the opening angle between clusters that form a candidate π^0 , a cut on the energy of the CB excluding the tunnel region, and a cut that selects π^- from TOF data. These cuts did not have strong impacts on the cross sections. The TOF cut was not only used to suppress backgrounds, but also to improve beam normalization as described in Sec. III C. All tests used in reconstruction of π^0 s are listed in Table I. For events that passed all cuts, the center-of-mass (c.m.) scattering angle of the π^0 was calculated and histogrammed into 20 bins of $\cos \theta_{c.m.}$.

B. Monte Carlo and acceptance

Two Monte Carlo simulation programs were used in the analysis, both of them based on GEANT 3 [16]. The first program (BEAMLIN) simulated the passage of beam particles along the beam path. It was used for beam normalization studies as described in Section III C. The BEAMLIN program provides a simple simulation with only a few elements along the beam path, and it tracks particles only inside a small tube along the beam axis. Our main simulation program CBALL includes a very detailed description of the experimental setup: all 672 crystals, the

CB enclosure, the target assembly, the beam pipe, the veto barrel, and all scintillation counters in the trigger were included in the simulation.

The CBALL simulation played a very important role in the analysis. In addition to the usual purpose of Monte Carlo simulations, to gain insight and confidence in the performance of the experimental setup, it was used to calculate the acceptance and the ratio of acceptances (ϵ and r_ϵ from Eq. 5), to evaluate the fraction of events that would trigger the veto system (VB calibration), and to calibrate the beam momentum as discussed in Sec. III D. Included in the input data for CBALL were distributions of CEX interaction points in the target and distributions of energies and directions of π^0 s and neutrons. These input quantities were provided by a separate kinematics program DECKIN. This program selected interaction points randomly from among the measured beam trajectories saved from experimental data. The directions of π^0 s were also selected randomly from a given angular distribution. The polar angular distribution was either flat (for final acceptance calculation) or given by a recent GWU partial-wave analysis (for momentum calibration). The remaining CBALL input, energies of π^0 s and the energies and directions of neutrons, were calculated from two-body kinematics by using as input a distribution of π^- momenta. The central value of the π^- momentum was input, and the distribution around that central value was obtained from experimental data. Energy loss in the target was included in the above calculations.

The two photons from π^0 decay and the neutron were tracked by CBALL through all elements on which they were incident and the deposited energies were recorded. For crystals, energies recorded with the pulser trigger were randomly added to simulate accidental backgrounds. The Monte Carlo events generated in this way were then analyzed in the same way as the real data with the exception of the TOF cut, see Sec. III A. Distributions of invariant mass and missing mass for real and Monte Carlo data of momentum 130 MeV/ c are shown in Fig. 2. The acceptance for a given bin was the ratio of the number of events that passed all cuts to the number generated. It is shown in Fig. 3 for the momentum 178 MeV/ c . The ratio of acceptances for scattering on carbon nuclei in the CH2 and carbon targets, r_ϵ , was also calculated from Monte Carlo data. As stated in connection with the correction factor F in Sec. III, average π^- momentum in the carbon target was lower than the one in the CH2 target. This difference in average momenta affected r_ϵ through the momentum dependence of the missing mass cut, but even if the target thicknesses were chosen such that average π^- momentum was the same in both targets, r_ϵ would still be needed because photons from the π^0 decay would still travel through the materials of different density. The values for r_ϵ ranged from about 0.94 to about 0.99 going from the lowest to the highest momentum.

The two photons could convert to e^+e^- or the neutrons could interact hadronically before traversing the veto barrel. Such events were rejected by the veto barrel if the energy deposited exceeded the threshold. The veto barrel calibration and a discussion on reliability of Monte Carlo simulations is described in [12].

C. Beam normalization

The number of beam particles B was known at the position of SB (30 cm upstream from the target) because a coincidence between S1, ST, and SB was a trigger requirement. Not all of these beam particles were pions because the beam was contaminated with muons and electrons. To obtain the number of pions that hit the target ($N_{\pi^-}^T$, $T = CH2, C, E$ from Eq. 5), one needs to find the fraction of pions in the beam at SB and the fraction of pions that survived from SB to the target. The fraction of pions in the beam at SB was determined with the TOF method because electrons, muons, and pions differ in time of flight between S1 and SB. The so-called decay muons cannot be distinguished from pions in this way. Decay muons originate from beam pion decays after the last beam channel magnet and thus fall under the pion S1-SB TOF peak. Contributions of decay muons to the pion TOF peak were determined from Monte Carlo simulations. Monte Carlo simulations were also used to obtain the fraction of pions that survived from SB to the target.

Taking all the above considerations into account, the number of pions that hit the target, corrected for computer live time, was evaluated as

$$N_{\pi^-} = B \cdot l \cdot f_{TOF} \cdot f_\pi \cdot s, \quad (7)$$

where B is the number of beam particles that hit SB (and S1 and ST), l is computer live-time correction, f_{TOF} is the fraction of particles in the pion peak of the S1-SB TOF spectra, f_π is fraction of pions in the pion TOF peak, and s is pion survival rate from SB to target. The computer live-time correction was calculated as the ratio of collected and triggered events, that is

$$l = \frac{\text{neutral events}}{\text{neutral triggers}}. \quad (8)$$

The TOF analysis was done by fitting the total S1-SB TOF spectrum with TOF spectra that included only electrons, muons, or pions. Samples of electrons, muons, and pions could be obtained by appropriate cuts on TOF spectra from

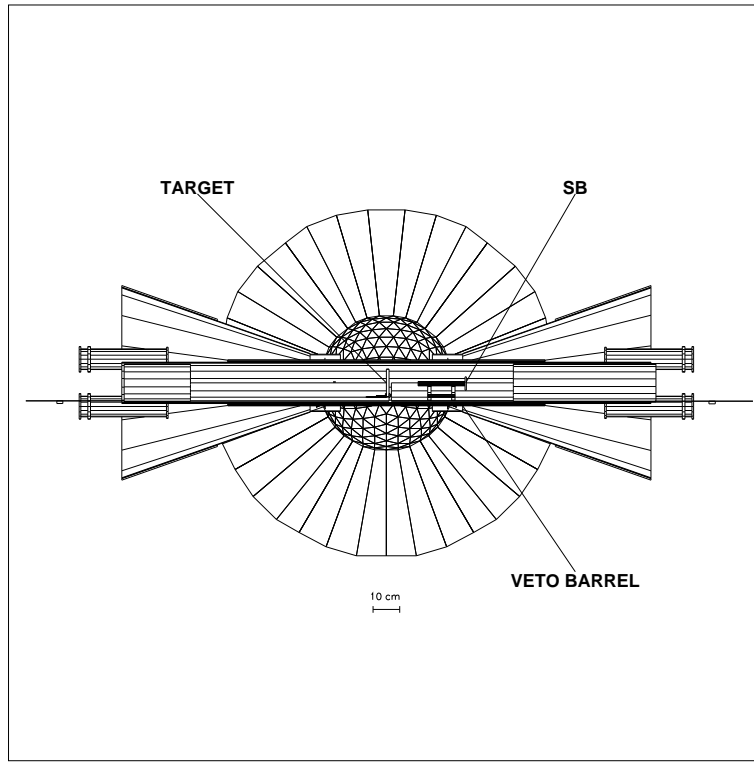


FIG. 1: The section of the Crystal Ball detector along the beam axis and including other elements of the experimental setup such as the target, the SB counter, and the veto barrel.

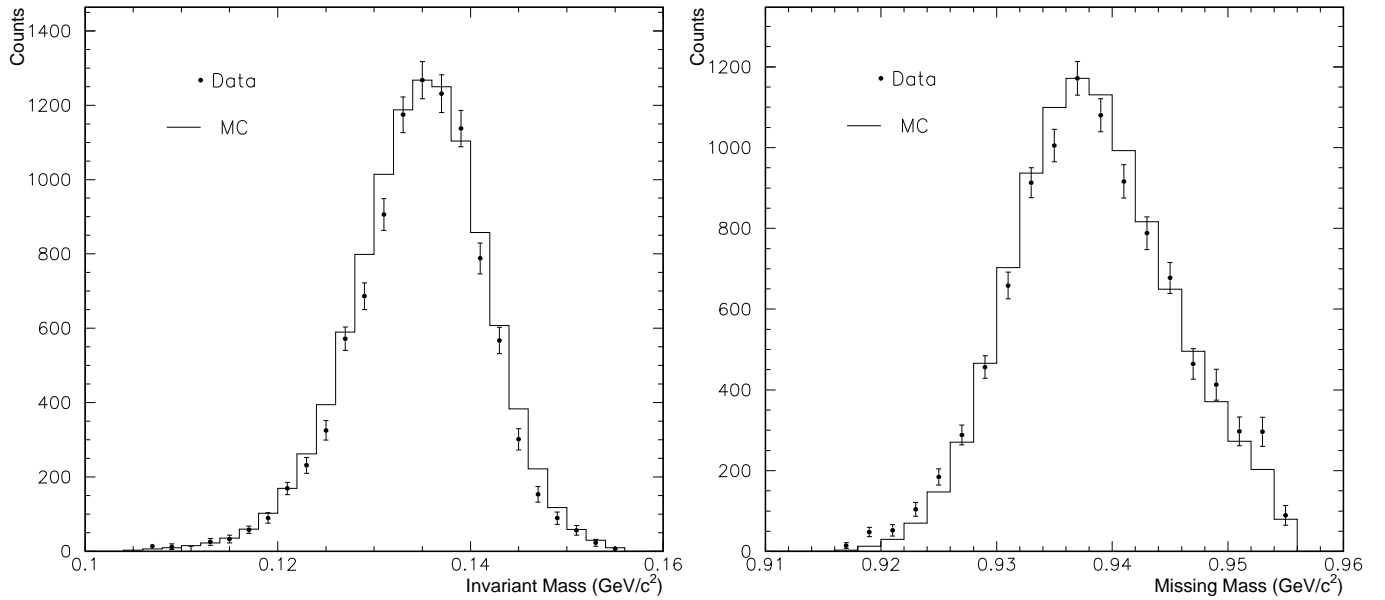


FIG. 2: Comparison between real and Monte Carlo data for momentum $130 \text{ MeV}/c$ of the invariant-mass and missing-mass distributions for pairs of clusters reconstructed to come from π^0 decays. The normalized empty and carbon target subtractions were applied to real data.

other TDCs, BVS for example. In addition, signals from the Čerenkov counter were used as a flag for electrons, and a signature for a CEX reaction was a flag for pions. Various combinations of electron, muon, and pion samples obtained in these ways were used to get a good understanding of systematic uncertainties.

The TOF spectra of the electron, muon, and pion samples were found to be asymmetric peaks with long tails towards increasing mass. This fact means that electrons contributed to the muon peak and both electrons and muons contributed to the pion peak, but that the electron peak consisted almost entirely of electrons. Thus the procedure was defined as follows. The total TOF spectrum was fitted with the electron TOF spectrum in the region of electron dominance. The yield for the fitted electron spectrum divided by yield for the total spectrum represents the fraction of electrons in the beam. The fitted electron spectrum was then subtracted from the total spectrum. The remaining spectrum had only muon and pion peaks, and a region dominated by muons. That region was fitted with the muon TOF spectrum. As for electrons, the yield for the fitted muon spectrum divided by the yield for the total spectrum represents the fraction of muons in the beam. Having the electron and muon fractions gave the pion fraction. The fitted electron and muon TOF spectra for 120 MeV/c are shown in Fig. 4 as shaded and black distributions, respectively, together with the total S1-SB TOF spectrum.

To reduce the systematic uncertainty of f_{TOF} , the pion fraction was determined only in the region dominated by pions. In Fig. 4, this region is on the right side of the vertical line. Thus f_{TOF} is a product of two factors. The first factor is the ratio of the number of events that had S1-SB TOF in the so-defined pion region to the total number of events. It was easily calculated and it only had a statistical uncertainty. The second factor is the fraction of pions in the defined pion region where the method described above was used to exclude decay muons. Results for this latter number were very stable over different sets of data and for all except the highest momenta, varying between 0.97 and 0.98. For the highest momenta, it was about 0.96. Calculating the pion fraction for only the pion region also means that the same cut had to be applied for the cross-section calculation. The cut eliminated only a small fraction of otherwise good candidates.

As mentioned, the BEAMLIN simulation program was used to determine the contribution of decay muons and the fraction of pions that survived from SB to the target. Input for this program was a *beam profile*, a value of the average (central) beam momentum, initial position of the beam, and the type of particle. By beam profile we refer to distributions of the positions (in a plane perpendicular to beam path), directions, and momenta (relative to the central momentum) of the beam particles. This information was obtained from the drift chambers for real data. Drift chambers were situated about 280 cm upstream from the target, so that position was chosen to be the initial position of the beam simulation. From there, generated pions were tracked to the target. Because the beam requirement was in the trigger, only events with pion or muon hits both in ST and SB were used in the analysis. To check the influence of the beam profile on the final results, simulations were done separately by using beam profiles from individual runs. All differences found were within statistical uncertainties. Also, for every beam profile, two simulations that had different values of the average beam momentum were done. The average beam momenta at the initial position differed by 3 MeV/c and were chosen to be around momenta obtained by momentum calibration.

Results for f_π obtained by averaging simulations with beam profiles from all runs are shown in Fig. 5 as a function of pion momentum at SB. In the same way as for f_π , results for s are shown in Fig. 6. Also in Fig. 6 is shown with a solid curve the theoretical fraction of pions that do not decay from SB to target given by

$$\frac{\pi_T^{th}}{\pi_{SB}^{th}} = \exp\left(-\frac{m d}{c\tau p}\right), \quad (9)$$

where c is the speed of light, τ is pion mean life, m is pion mass, d is the distance between SB and target, and p is average pion momentum between SB and target. The difference between curve and survival rate represents scattered pions.

D. Beam momentum calibration

Beam momenta were obtained in three independent ways, which we call the previous calibration, calibration with invariant mass and missing mass (IM-MM calibration), and calibration with time-of-flight (TOF calibration).

The momentum calibration of the C6 beam line was checked extensively in previous experiments including ones by our collaboration [12, 15, 17]. The beam momentum was thus approximately known at the position of the last dipole magnet, D2. A value of beam momentum at the target center can then be calculated by using this value as input for an energy-loss calculation. The main problem with this procedure is that previous beam-line calibrations were performed at higher momenta and then simply extrapolated to the momentum range of the current experiment, which can induce unknown systematic uncertainties.

The IM-MM calibration was based on comparing the invariant-mass and the missing-mass distributions for the real and Monte Carlo data. The average π^- momentum at the target center was not known in the raw real data but could

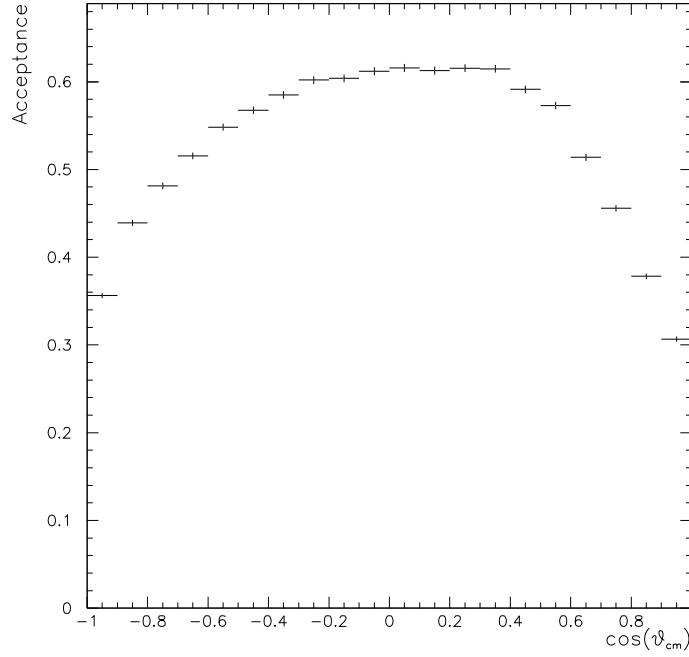


FIG. 3: Acceptance for momentum 178 MeV/c.

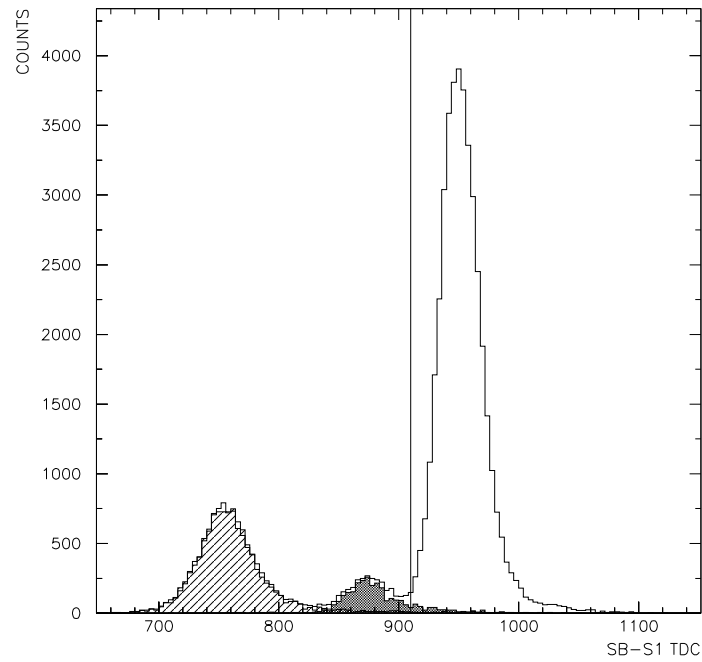


FIG. 4: The difference between SB and S1 TDC values for data with π^- momentum 120 MeV/c and the CH2 target. The three peaks from left to right are from electrons, muons, and pions, respectively. Fits to the electron and muon samples are shown as shaded and black distributions, respectively. The position of the cut that selects the pion region is shown by a vertical line.

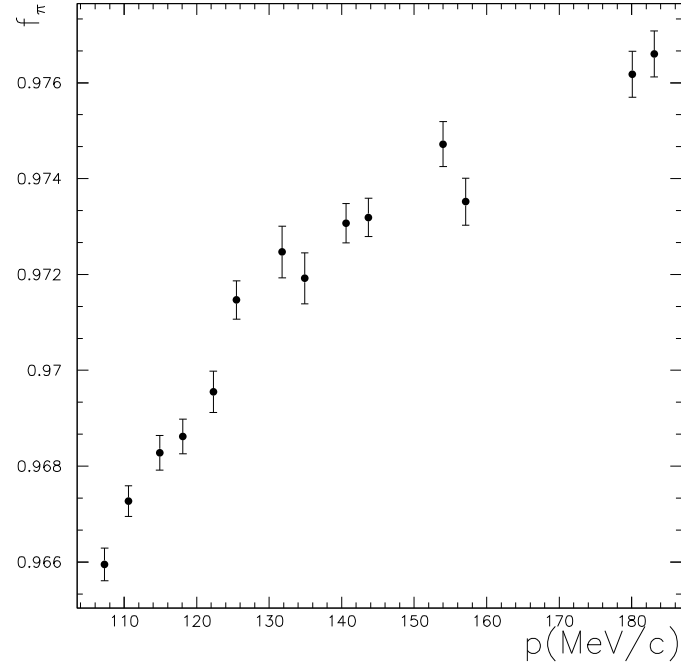


FIG. 5: Fraction of pions in the set of particles with pion TOF at the position of SB, f_π from Eq. 7, as a function of pion momentum at SB. Statistical uncertainties are shown with error bars.

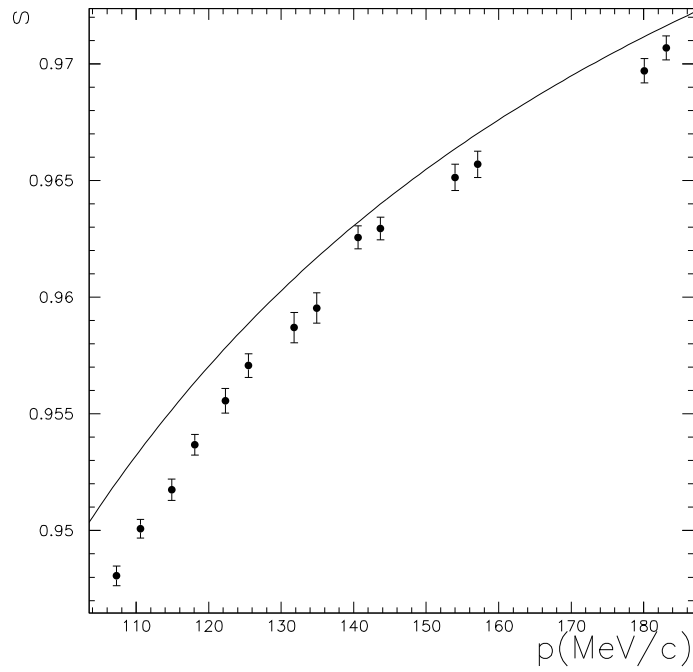


FIG. 6: Survival rate of pions from SB to target, s from Eq. 7, as a function of pion momentum at SB is shown with statistical uncertainties. The theoretical fraction of pions that do not decay in flight from SB to target is shown by a solid curve.

TABLE II: Momentum calibration. The first two columns are the nominal and corrected momenta at D2. In third column are momenta at the target center obtained with a previous D2 magnet calibration and energy loss calculations, with input from the second column. The last two columns are momenta at the target center from the IM-MM calibration, and calibration from the TOF method. The TOF calibration can not be used for the two highest momenta.

P_{D2}	P_{D2} corr.	Prev. P_T	IM-MM P_T	TOF P_T
119	117.5	107.2	103.0	105.2
126	126.0	116.9	112.4	113.3
132	131.3	122.8	120.0	121.4
140	140.2	132.5	129.6	131.4
148	148.5	141.4	139.2	139.6
161	161.0	154.6	152.0	-
186	186.4	179.9	178.1	-

be assumed for the analysis. The missing-mass distribution depends on the assumed value of the π^- momentum. For small relative changes, the dependence is linear. On the other hand, missing mass for the Monte Carlo data does not depend (or depends very weakly) on the beam momentum. The actual momentum is then equal to the assumed momentum for which real and Monte Carlo missing-mass distributions are equal. For this procedure to be justified, real and Monte Carlo data have to be in good agreement. In particular, they have to have the same distribution in π^0 polar angle and they have to be gain-matched in CB energy. The procedure was as follows. Real distributions for invariant and missing mass were generated with the same cuts and background subtractions that were used for obtaining cross sections. Monte Carlo events, generated with the same cuts, were distributed in polar angle as predicted by the recent GWU analysis. Energy gain-matching was done so that real and Monte Carlo invariant mass peaks match. This match can be done either by adjusting the overall gain of the NaI crystals or the corresponding parameter in the Monte Carlo analysis. After real and Monte Carlo data were matched, the positions of the peaks in the missing-mass spectra were found with Gaussian fits for several different values of beam momentum. The uncertainty of this procedure was found to be

$$\sigma_P \approx 5\sigma_M, \quad (10)$$

where σ_P is the momentum uncertainty in MeV/c and σ_M is the uncertainty in the peak position of the mass distributions in MeV/c². The uncertainty of the IM-MM calibration was estimated to be about 1.2 MeV/c.

In the TOF calibration, the theoretical and measured differences between pion and electron TOFs were compared. Electrons travel effectively at the speed of light so their TOF between two points on beam path is easily calculated. Pion TOF between the same two points was found for several different pion momenta, taking into account energy loss. In that way, a dependence between beam momentum and the difference in pion and electron TOFs was found. On the other hand, this difference was measured by finding (using Gaussian fitting) positions of pion and electron peaks in TOF spectra. The measured difference in TOF values suffers from two systematic uncertainties. The first source of uncertainty comes from an uncertainty of the precise value of the conversion factor between the time-to-digital converter (TDC) value and time. This uncertainty is not a limiting factor because a 1% uncertainty in the conversion factor leads to ≈ 0.8 MeV/c uncertainty in momentum. The second source of uncertainty is a known effect of electronic signal walk and it can be quite large. The uncertainty can be reduced by measuring TOF differences between several pairs of TDCs. The values of the S1 left and right TDCs were subtracted from: ST left and right, SB left and right, and the BVS TDC. The result is ten differences (six independent) in TDCs that were then used to form a weighted average where more weight was given to the differences in TDCs coming from the counters that were further apart. The exact procedure is not important because this method is less reliable than the IM-MM calibration method and it was used only as a consistency check. For the two highest momenta, the uncertainties of the procedure become too large to give useful results.

The average π^- momenta at the target center were calculated in these three ways and are shown in the last three columns of Table II. Momenta from the previous calibration are systematically higher than momenta obtained with the TOF analysis, and the TOF momenta are systematically higher than momenta from the IM-MM calibration. The difference between the previous calibration and IM-MM tends to increase with decreasing momentum. The IM-MM calibration was accepted as the most reliable. For the final results, IM-MM values (rounded to the nearest integer) and uncertainty estimate were used.

IV. RESULTS

A. Systematic uncertainties

The following sources of systematic uncertainties were identified: beam normalization, calibration of the veto barrel, difference between the densities of the CH2 and carbon targets, and small differences between real and Monte Carlo data (cut sensitivity).

The uncertainty in beam normalization, as seen from Eq. 7, comes from uncertainties of beam Monte Carlo simulations (0.4% - 0.2%), statistical uncertainties of computer live time (0.3% - 0.1%), and statistical (0.4% - 0.1%) and systematic uncertainties (0.3% - 1.0%) in the determination of the pion fraction, f_{TOF} . The overall contribution of beam normalization to the total uncertainty was estimated to be 0.7% - 1.8%. In the quoted ranges of uncertainties, the first number refers to the lowest momentum and second to the highest.

The uncertainty of the veto barrel calibration was estimated to be 2% for all momenta.

The difference between densities of the CH2 and carbon targets adds to the total uncertainty through the uncertainty in estimating the correction factor F and the uncertainty of r_ϵ . These two factors combined gave a 0.8% - 1.3% uncertainty.

Finally, the change in the total cross section with and without the missing-mass cut was a measure of systematic uncertainty coming from small differences between real and Monte Carlo data. For all momenta except the lowest, the uncertainty was about 1%, and for the lowest it was about 2.5%.

The total systematic uncertainty, obtained by adding in quadrature all of the described contributions, was close to 3% for all momenta. The results are summarized in Table III.

TABLE III: Sources of systematic uncertainties and total systematic uncertainty.

Momentum (MeV/c)	Kin. Energy (MeV)	Beam normalization	Veto barrel calibration	Difference in target densities	Cut sensitivity	Total uncertainty
103	33.9	0.7%	2.0%	0.8%	2.5%	3.4%
112	39.4	0.9%	2.0%	1.0%	1.0%	2.6%
120	44.5	1.0%	2.0%	1.1%	1.0%	2.7%
130	51.2	1.3%	2.0%	1.2%	1.0%	2.9%
139	57.4	1.4%	2.0%	1.3%	1.0%	2.9%
152	66.8	1.7%	2.0%	1.1%	0.8%	3.0%
178	86.6	1.8%	2.0%	0.8%	0.8%	2.9%

B. Cross sections

The obtained values of $\pi^- p \rightarrow \pi^0 n$ differential cross sections and their statistical uncertainties are listed in Tables IV and V.

They are also plotted in Figs. 7, 8, and 9 together with the results of the FA08 partial-wave analysis (PWA) of the George Washington group [18]. Statistical uncertainties range from 3% to 6% for the highest momentum, to 6% to 15% for the lowest momenta except for the few most forward-angle points of the lower momenta. Statistically significant differences between our results and PWA predictions are found. These differences vary with momentum and angle. The biggest difference, both in statistical significance and in size, is in the backward-angle region for momentum 139 MeV/c where it is about 10%. The size of the difference and its momentum and angle dependence are very unlikely to be explained by a single error in analysis, if such existed. In particular, note that the beam normalization, usually the strongest source of uncertainty, is very well controlled in this experiment.

The differential cross sections were fitted with an expansion in Legendre polynomials

$$\frac{d\sigma}{d\Omega} = \sum_{L=0}^{L_{\max}} A_L P_L(\cos \theta) \quad (11)$$

to obtain the total cross sections, where $\sigma_T = 4\pi A_0$. Only sums up to $L_{\max} = 2$ were needed for all momenta. The total charge-exchange cross sections are listed in Table VI together with statistical and total uncertainties. The Legendre coefficients and their uncertainties are listed in Table VII. The data are fitted very well within

TABLE IV: Differential cross sections.

Momentum $\cos \theta_{c.m.}$	103 MeV/c		112 MeV/c		120 MeV/c		130 MeV/c	
	$d\sigma/d\Omega$	uncertainty	$d\sigma/d\Omega$	uncertainty	$d\sigma/d\Omega$	uncertainty	$d\sigma/d\Omega$	uncertainty
-0.95	1.016	0.064	1.145	0.062	1.206	0.062	1.567	0.074
-0.85	0.987	0.056	1.045	0.055	1.294	0.054	1.469	0.066
-0.75	0.871	0.051	1.028	0.050	1.162	0.049	1.299	0.059
-0.65	0.820	0.047	0.892	0.044	0.979	0.045	1.129	0.053
-0.55	0.754	0.044	0.793	0.042	0.797	0.039	1.021	0.048
-0.45	0.714	0.041	0.798	0.040	0.776	0.037	0.857	0.043
-0.35	0.618	0.040	0.642	0.036	0.751	0.034	0.799	0.040
-0.25	0.539	0.034	0.593	0.033	0.588	0.031	0.640	0.037
-0.15	0.421	0.031	0.493	0.031	0.509	0.028	0.563	0.032
-0.05	0.421	0.030	0.429	0.028	0.459	0.027	0.545	0.030
0.05	0.415	0.028	0.387	0.025	0.417	0.024	0.430	0.028
0.15	0.275	0.025	0.318	0.024	0.325	0.022	0.368	0.026
0.25	0.245	0.023	0.232	0.023	0.239	0.021	0.286	0.022
0.35	0.223	0.022	0.201	0.021	0.202	0.019	0.227	0.020
0.45	0.188	0.021	0.149	0.019	0.154	0.016	0.140	0.018
0.55	0.132	0.020	0.138	0.017	0.081	0.015	0.130	0.018
0.65	0.125	0.019	0.064	0.015	0.111	0.015	0.086	0.014
0.75	0.097	0.015	0.056	0.014	0.048	0.012	0.070	0.014
0.85	0.062	0.014	0.045	0.013	0.043	0.011	0.030	0.012
0.95	0.015	0.011	0.014	0.011	0.008	0.010	0.020	0.012

TABLE V: Differential cross sections.

Momentum $\cos \theta_{c.m.}$	139 MeV/c		152 MeV/c		178 MeV/c	
	$d\sigma/d\Omega$	uncertainty	$d\sigma/d\Omega$	uncertainty	$d\sigma/d\Omega$	uncertainty
-0.95	1.938	0.063	2.157	0.073	3.010	0.081
-0.85	1.587	0.055	1.872	0.065	2.609	0.068
-0.75	1.564	0.050	1.768	0.057	2.454	0.062
-0.65	1.306	0.045	1.533	0.052	2.163	0.056
-0.55	1.155	0.041	1.353	0.046	1.875	0.050
-0.45	1.042	0.036	1.223	0.042	1.589	0.045
-0.35	0.878	0.032	1.021	0.039	1.311	0.041
-0.25	0.719	0.029	0.819	0.035	1.127	0.036
-0.15	0.622	0.027	0.717	0.031	0.899	0.033
-0.05	0.502	0.024	0.596	0.028	0.771	0.030
0.05	0.423	0.022	0.491	0.025	0.650	0.027
0.15	0.334	0.019	0.398	0.023	0.506	0.024
0.25	0.261	0.017	0.280	0.020	0.450	0.021
0.35	0.221	0.016	0.216	0.018	0.374	0.020
0.45	0.189	0.015	0.174	0.017	0.383	0.019
0.55	0.114	0.013	0.152	0.015	0.322	0.017
0.65	0.094	0.012	0.142	0.015	0.361	0.019
0.75	0.072	0.012	0.088	0.014	0.329	0.019
0.85	0.046	0.011	0.114	0.014	0.339	0.020
0.95	0.038	0.011	0.100	0.015	0.369	0.024

their uncertainties by Eq. 11. The statistical and systematic uncertainties were added in quadrature for the total

TABLE VI: The total charge-exchange cross section obtained from integrating the differential cross section with statistical and total uncertainties.

Momentum (MeV/c)	Total cross section (mb)	Statistical uncertainty	Total uncertainty
103	5.61	0.10	0.22
112	5.96	0.09	0.18
120	6.39	0.09	0.19
130	7.33	0.11	0.24
139	8.21	0.09	0.26
152	9.58	0.10	0.30
178	13.75	0.11	0.41

TABLE VII: Legendre coefficients, with uncertainties in parentheses, from fits to the differential cross section data.

Momentum (MeV/c)	A_0	A_1	A_2
103	0.4463 (0.0078)	-0.540 (0.015)	0.110 (0.014)
112	0.4747 (0.0074)	-0.627 (0.014)	0.156 (0.013)
120	0.5081 (0.0071)	-0.695 (0.014)	0.192 (0.013)
130	0.5830 (0.0084)	-0.813 (0.016)	0.245 (0.015)
139	0.6532 (0.0070)	-0.946 (0.014)	0.346 (0.012)
152	0.7623 (0.0081)	-1.090 (0.016)	0.452 (0.015)
178	1.0939 (0.0089)	-1.361 (0.017)	0.729 (0.018)

uncertainty. The results are shown in Fig. 10 and compared to the GWU FA08 partial-wave analysis and to the previous data [7, 8, 12, 14, 19]. As expected from the differential cross sections, our results agree with PWA predictions for the momentum 178 MeV/c, and are higher than predictions for the other momenta.

C. Consistency Checks

The results of the analysis were carefully examined to identify any issues that might not already be covered by the known systematic uncertainties. The first one has already been mentioned. Although the GWU partial-wave predictions systematically disagree with the data at the backward angles, as seen in Figs. 7 to 9, the Legendre expansion provides an excellent representation at all momenta with no need for terms beyond $P_2(\cos\theta)$, see Fig. 11 for example. Furthermore, as shown in Fig. 12, the Legendre coefficients each have a smooth dependence on momentum. These data can also be very well represented within the error bars by quadratic or cubic polynomial fits. Such fits, however, are not reliable much outside the momentum range of the data. Partial-wave codes are needed for such extrapolations.

The smooth behavior of the Legendre coefficients gives confidence that there are no significant momentum-dependent concerns in the data. The A_0 coefficient provides values for the total cross sections. As seen in Fig. 10, the results of our experiment are consistent with those of other experiments, and generally have smaller uncertainties.

A final consistency check is the location of the minimum in the 0° cross section, which arises from the interference of s and p waves. Although our error bars for these cross sections are larger than those of Jia *et al.* [13], we find the minimum cross section to be at 41.8 ± 1.1 MeV (116.0 MeV/c) as compared to 41.9 ± 0.9 MeV for Jia *et al.*. The GWU FA08 solution yields $\simeq 46$ MeV.

V. CONCLUSION

Differential cross sections of the charge-exchange reaction $\pi^- p \rightarrow \pi^0 n$ are presented for seven momenta in the range from 103 to 178 MeV/c. Complete angular distributions were obtained by using the Crystal Ball detector. The results presented here almost double the existing database in the low-energy region. The obtained cross sections are higher in the backward-angle region than the predictions of the GWU FA08 partial-wave analysis based on earlier experiments. These data could have an important impact on investigations of isospin breaking at low energies. They will also be useful for extracting important physical quantities such as the πN σ term.

Acknowledgments

This work was supported in part by the U.S. DOE and NSF, by the Croatian MZOS, by the Russian Foundation for Basic Research, and by NSERC of Canada. The assistance of BNL and AGS with the setup is greatly appreciated.

-
- [1] W. R. Gibbs, L. Ai, and W. B. Kaufmann, Phys. Rev. Lett. **74**, 3740 (1995).
 - [2] E. Matsinos, Phys. Rev. **C56**, 3014 (1997).
 - [3] E. Matsinos, W. S. Woolcock, G. C. Oades, G. Rasche, and A. Gashi, Nucl. Phys. **A778**, 95 (2006), hep-ph/0607080.
 - [4] N. Fettes and U.-G. Meissner, Phys. Rev. **C63**, 045201 (2001), hep-ph/0008181.
 - [5] A. B. Gridnev, I. Horn, W. J. Briscoe, and I. I. Strakovsky, Phys. Atom. Nucl. **69**, 1542 (2006), hep-ph/0408192.
 - [6] P. Schweitzer, Phys. Rev. **D69**, 034003 (2004), hep-ph/0307336.
 - [7] M. Salomon, D. F. Measday, J. M. Poutissou, and B. C. Robertson, Nucl. Phys. **A414**, 493 (1984).
 - [8] A. Bagheri et al., Phys. Rev. **C38**, 875 (1988).
 - [9] D. H. Fitzgerald et al., Phys. Rev. **C34**, 619 (1986).
 - [10] L. D. Isenhower et al., PiN Newslett. **15**, 292 (1999).
 - [11] E. Frlež et al., Phys. Rev. **C57**, 3144 (1998), hep-ex/9712024.
 - [12] M. E. Sadler et al. (Crystal Ball), Phys. Rev. **C69**, 055206 (2004), nucl-ex/0403040.
 - [13] Y. Jia et al., Phys. Rev. Lett. **101**, 102301 (2008), 0804.1531.
 - [14] J. Breitschopf et al., Phys. Lett. **B639**, 424 (2006), nucl-ex/0605017.
 - [15] A. Starostin et al. (Crystal Ball), Phys. Rev. **C64**, 055205 (2001).
 - [16] GEANT 3.21 CERN program library long writeup W5013, CERN, Geneva, Switzerland.
 - [17] W. B. Tippens et al., Phys. Rev. **D63**, 052001 (2001).
 - [18] R. A. Arndt, W. J. Briscoe, I. I. Strakovsky, and R. L. Workman, Phys. Rev. **C74**, 045205 (2006), nucl-th/0605082.
 - [19] D. V. Bugg et al., Nucl. Phys. **B26**, 588 (1971).

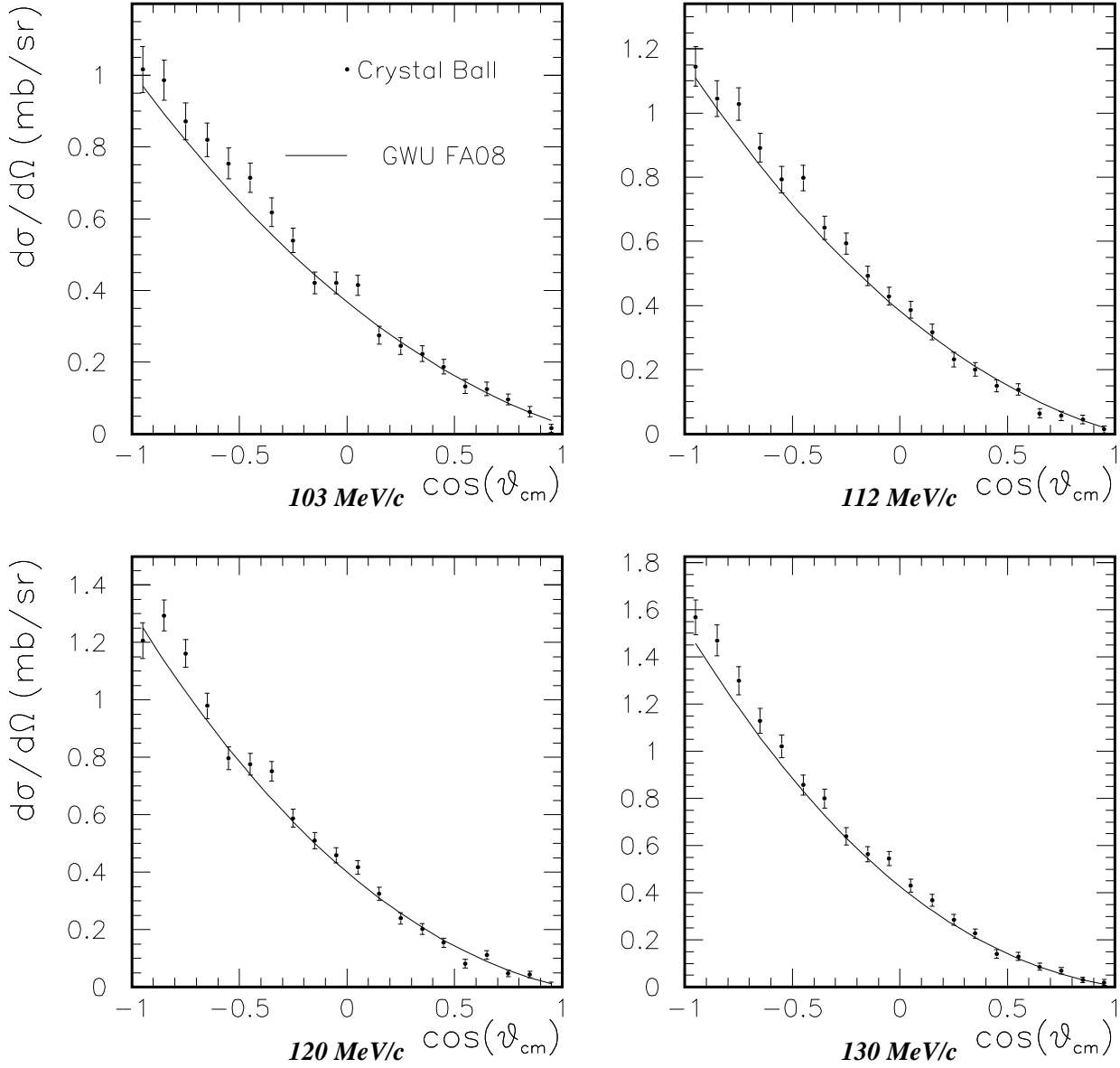


FIG. 7: Differential cross sections of reaction $\pi^- p \rightarrow \pi^0 n$. Black circles are the values obtained in this experiment with the error bars showing statistical uncertainties. The curves are the results of the FA08 partial-wave analysis of the George Washington group [18].

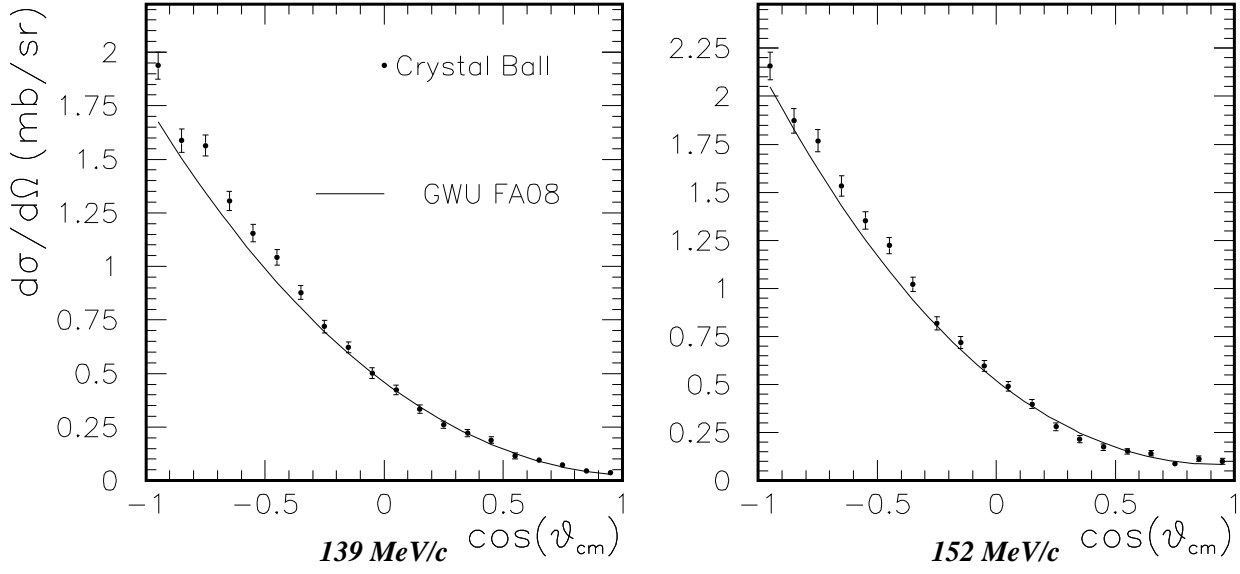


FIG. 8: Differential cross sections for the reaction $\pi^- p \rightarrow \pi^0 n$. Black circles are the values obtained in this experiment, with the error bars showing statistical uncertainties. The curves are the results of the FA08 partial-wave analysis of the George Washington group [18].

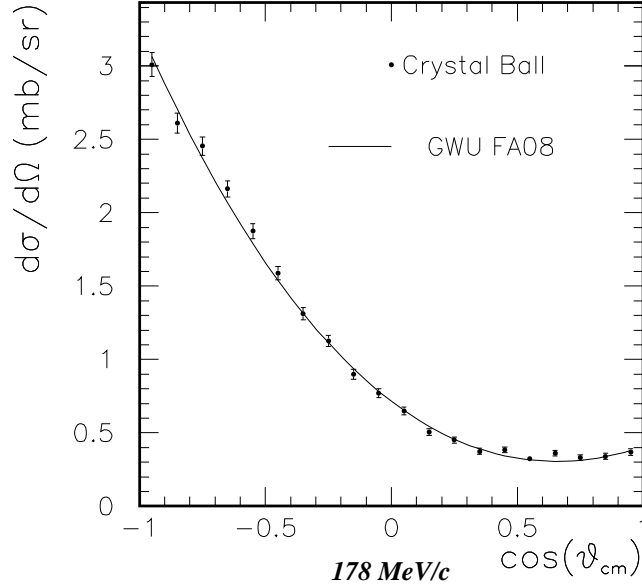


FIG. 9: Differential cross sections of the reaction $\pi^- p \rightarrow \pi^0 n$. Black circles are the values obtained in this experiment with the error bars showing statistical uncertainties. The curves are the results of the FA08 partial-wave analysis of the George Washington group [18].

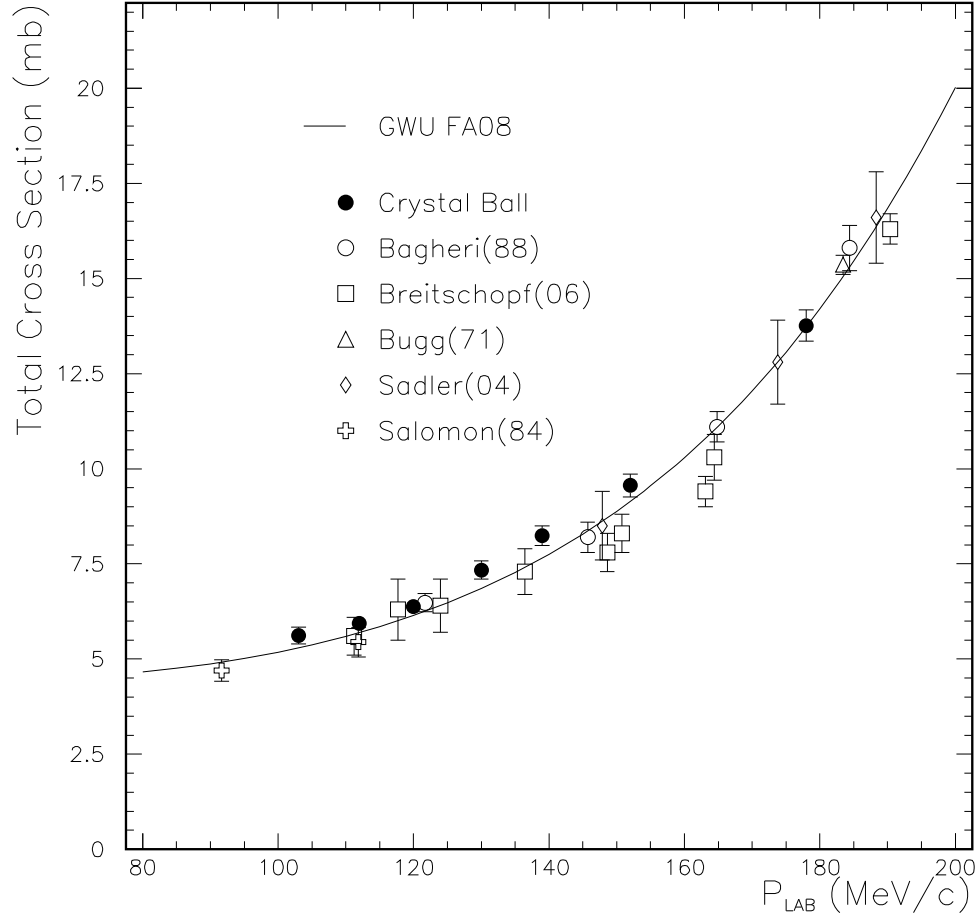


FIG. 10: The total charge-exchange cross sections obtained from integrating the differential cross sections. The error bars show combined statistical and systematic uncertainties. The results are compared to the GWU FA08 partial-wave analysis [18] and to previous data [7, 8, 12, 14, 19].

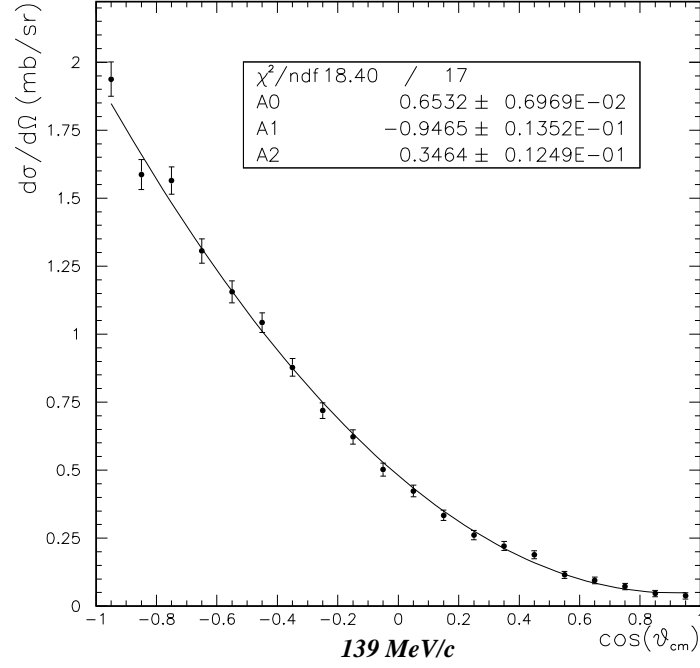


FIG. 11: Fit of the differential cross section for 139 MeV/c with an expansion in Legendre polynomials up through $L = 2$. Values of the χ^2 of the fit and Legendre coefficients A_0 , A_1 , and A_2 are shown.

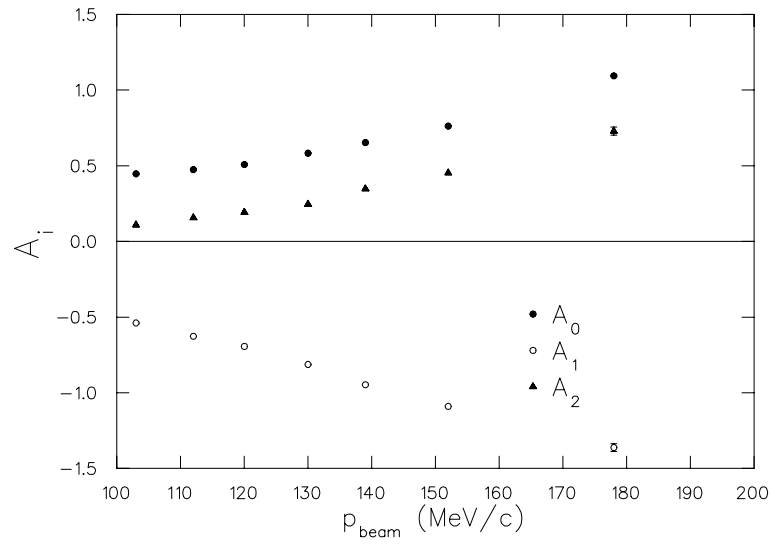


FIG. 12: Legendre coefficients from fits to the differential cross section data.